

Wireless charging Class-E inverter for zero-voltage switching over coupling coefficient range

Anon Namin¹, Chuchat Donloei¹, Ekkachai Chaidee²

¹Department of Electrical Engineering, Faculty of Engineering, Rajamangala University of Technology Lanna, Chiang Mai, Thailand

²Department of Electrical Engineering, Faculty of Engineering, Rajamangala University of Technology Lanna, Chiang Rai, Thailand

Article Info

Article history:

Received Feb 5, 2025

Revised May 12, 2025

Accepted May 25, 2025

Keywords:

Class-E inverter

Magnetic coupling coefficient

Misalignment

Wireless power transfer system

Zero voltage switching

ABSTRACT

A novel and practical methodology is presented in this study for designing contactless wireless energy systems using resonant-mode Class-E converters, aiming to sustain efficient soft-transition switching under various levels of magnetic coupling, even under coil misalignment. The approach integrates the wireless power transfer (WPT) circuit with the inverter's series resonant network and analytically derives the relationship between the coupling coefficient and impedance phase angle to identify zero voltage switching (ZVS) conditions. A key contribution is the use of the maximum expected coupling coefficient as a critical design point to ensure ZVS across practical variations. A complete step-by-step design procedure is provided. Simulation and experimental results confirm that the inverter achieves and maintains ZVS for coupling values in the range $0 < k \leq k_{\text{designed}}$, with efficiencies reaching up to 95%. This work supports the advancement of soft-switching inverter design to enable robust and efficient WPT systems under practical misalignment conditions.

This is an open access article under the [CC BY-SA](#) license.



Corresponding Author:

Ekkachai Chaidee

Department of Electrical Engineering, Faculty of Engineering

Rajamangala University of Technology Lanna

99, Moo 10, Sai Khao Sub-district, Phan District, Chiang Rai 57120, Thailand

Email: ekkachai@rmutl.ac.th

1. INTRODUCTION

Recently, wireless charging technology has seen widespread adoption across various application areas, including biomedical implants [1]-[3], small-scale electronic equipment [4], [5], and power wheelchairs [6], [7]. For high-power applications, it is also used in electric vehicles (EVs) [8]-[10]. Enhancing both safety and convenience, wireless power transfer presents a notable advancement over traditional wired charging methods.

Within a wireless charging setup, the inverter serves as a key component by transforming direct current (DC) power into high-frequency AC signals. This high-frequency AC energizes the primary coil to generate a fluctuating magnetic field, which induces voltage in the secondary side. Wireless charging systems utilize different inverter configurations, including full-bridge [11], half-bridge [12], and Class-E inverters, which were initially introduced in [13]. Utilizing a full-bridge inverter necessitates four switching devices, which increases the overall component count, cost, and associated power losses. Additionally, achieving zero-voltage switching (ZVS) with this topology poses considerable challenges [14], [15]. In contrast, the half-bridge inverter reduces the number of power switches and related circuitry by half, thereby simplifying the design and mitigating these issues. Nonetheless, this configuration typically results in a reduction of the system's rated output power.

Due to its efficient performance, compact structure, and economic viability, the Class-E inverter has gained considerable attention in wireless power transfer (WPT) applications. This is due to its use of a single switch, which is capable of operating under ZVS conditions, which minimizes energy dissipation during switching and reduces stress on the switch. This type of inverter can be applied in wireless power transfer systems. However, its operation may deviate from ZVS conditions, particularly because of the unavoidable misalignment between coils in practical operations. Previous research efforts have attempted to address this drawback.

Previous study [16], an improved Class-E configuration is designed to maintain a stable output current and maintain ZVS under varying loads. However, the impact of magnetic coupling variations was not addressed. Previous study [17], a Class-E configuration tolerant to load variations and equipped with parallel resonance enables zero-voltage switching by ensuring switch voltage falls to zero before turn-on, regardless of load variations. Previous study [18], ZVS is achieved using a Class-E² structure with three inductors in a push-pull arrangement and LCC-S tank, enabling wide-range load-independent switching without active feedback. In [19], [20], an introduction to a Class-E converter is provided, designed to address the high voltage stress issues in the WPT systems. By incorporating a supplementary circuit into the converter, the introduced topology significantly reduces voltage stress and switching losses, while also achieving zero-voltage switching (ZVS) conditions to ensure efficient power transfer. He and Guo [21] proposed using impedance matching and a searching algorithm to combine a series/parallel capacitor array to tune the Class-E inverter operation, bringing it back to the optimal state for different coil distances. As well as [22], this paper proposed a tuning method by adjusting the phase angle of the series resonant branch with pulse width modulation capacitor on the transmitter side. Ahmadi *et al.* [23] introduced a method for achieving ZVS in Class-E inverters for the WPT systems utilizing series-series compensation. This is accomplished by connecting a compensation switch across the secondary side capacitor. By controlling the ON/OFF state of this switch, the secondary circuit parameters can be varied to satisfy the ZVS condition. As well as, in [24] used reconfiguration of the receiver circuit by a switched-capacitor to achieve the ZVS condition under variation of load. The result in [25], a modified PSO-based method was proposed for designing Class-E switching circuits. While WPT is noted as a potential application, the method is not implemented in a WPT system. ZVS in an inverter based on Class-E topology applied to CWPT can be realized by tuning LC resonant components and compensating load reactance with external inductors or capacitors [26]. However, the study does not address IPT systems. An off-nominal Class-E amplification was utilized to attain ZVS by allowing a nonzero voltage slope at turn-on [27]. However, the method was not applied to wireless power transfer. A Class-E-based WPT configuration insensitive to load variations was introduced to enable zero-voltage switching without control, using dual-resonance and constant reactance via proper receiver tuning and Class-D rectification [28]. The method was validated in a multihop robotic arm system. An inverter based on Class-E topology, along with a Class-DE rectification stage, was utilized in developing a WPT system for biomedical implants, with ZVS achieved through circuit design [29].

In [16]-[24], achieving ZVS conditions relies on circuit reconfiguration or the addition of extra components. In contrast, [25]-[29] achieve ZVS through inherent design approaches. However, comprehensive design guidelines for ensuring ZVS in wireless power transfer applications, especially under coil misalignment, remain limited. This paper addresses this gap by presenting a detailed analysis and design methodology for Class-E inverters in WPT systems, ensuring reliable ZVS operation under misalignment without additional tuning or control. The proposed approach employs the maximum expected coupling coefficient as a key design parameter and is validated through both simulation and experimental results.

The structure of this paper begins with an overview of methods and design approaches in section 2, followed by validation through simulations and experiments in section 3, followed by concluding insights discussed in section 4.

2. METHOD

This section presents an in-depth analysis of a system for wireless power delivery integrated with a Class-E topology. The focus is on identifying the regions of zero voltage and non-zero voltage based on the magnetic coupling coefficient, deriving component design equations, providing a demonstrative design case study, and elucidating the various operational modes of the system.

2.1. Circuit analysis

This section analyzes the impedance behavior within a WPT arrangement, emphasizing the relationship between impedance phase angle and magnetic coupling coefficient, enabling the identification of ZVS and non-ZVS conditions. ZVS is crucial for reducing switching losses and enhancing system efficiency. This analysis provides valuable insights for determining optimal design parameters. The assumptions underlying the circuit analysis in this section are as follows:

- A switch operates at a duty cycle of 0.5.

- The switching device has a zero-turn-on resistance.
- The resonant network has a sufficiently high quality factor, ensuring the current through the WPT system is sinusoidal.
- The large choke inductance allows the current ripple to be neglected, and the choke inductor's DC resistance is disregarded.
- The choke inductor's self-capacitance and parasitic capacitance are included in the shunt capacitance of the switch.

2.1.1. Impedance analysis in Class-E inverter-based wireless power transfer systems

Figure 1(a) illustrates a typical Class-E resonant inverter circuit. Its components include DC input voltage (V_1), a choke inductor (L_f), and an electronic switch (S). Parallel to the switch is a shunt capacitance (C_1), which incorporates both the stray capacitance of the switching device and the intrinsic capacitance for the choke inductor. The inductance L_0 forms a series path alongside resonant capacitor C_0 and load resistance R , forming a resonant network that satisfies the resonance condition. To apply the inverter with the WPT system, the resistive load (R) in Figure 1(a) is replaced by the wireless power system, depicted in Figure 1(b). The components of WPT circuit include primary inductance (L_p) and secondary inductance (L_s) of the coil, a secondary capacitance (C_s) used to cancel the secondary leakage inductance under resonant conditions, diodes (D_1 - D_4) acting as a rectifier circuit that transforms high-frequency AC into DC, a filter capacitor (C_f), and the load resistance (R_L). In practice, the resonant tank (L_0) can be included with the primary inductance (L_p) to become a single inductance, and using the capacitance (C_0) to cancel the primary leakage inductance, thereby reducing the reliance on an extra coil and capacitance.

The equivalent resistance seen from the rectifier circuit to R_L , as shown in Figure 1(b), can be expressed by (1), and the secondary-side impedance can be defined by (2).

$$R_{Leq} = \frac{8R_L}{\pi^2} \quad (1)$$

$$Z_2 = R_{Leq} + j\left(\omega L_s - \frac{1}{\omega C_s}\right) - j\omega M \quad (2)$$

As depicted in Figure 1(b), the circuit is simplified into an equivalent form, which is modeled in Figure 1(c), with the reflected impedance Z_r defined in (3).

$$Z_r = \frac{(\omega M)^2}{R_{Leq} + jX_s} \quad (3)$$

Thus, the corresponding circuit, illustrated in Figure 1(b), is converted into the configuration depicted in Figure 1(c). The WPT system's input impedance (Z_{in}) is determined by $Z_r + j\omega L_p$, as expressed in (4).

$$Z_{in} = \frac{(\omega M)^2 - \omega L_p X_s + j\omega L_p R_{Leq}}{R_{Leq} + jX_s} \quad (4)$$

The circuit in Figure 1(d) is a simplified version of the circuit in Figure 1(c). The impedance Z_{Ti} , as seen in Figure 1(d), is determined by the expression $(Z_r + j\omega L_p) + j\left(\omega L_0 - \frac{1}{\omega_0 C_0}\right)$. The impedance Z_{Ti} can be separated into its real R_{Ti} and imaginary parts X_{Ti} , as expressed in (5)-(7).

$$Z_{Ti} = R_{Ti} + jX_{Ti} \quad (5)$$

$$R_{Ti} = \frac{(\omega M)^2 R_{Leq}}{R_{Leq}^2 + X_s^2} \quad (6)$$

$$jX_{Ti} = \frac{j[(R_{Leq}^2 + X_s^2)(\omega L_p + jX_0) - X_s(\omega M)^2]}{R_{Leq}^2 + X_s^2} \quad (7)$$

The equivalent impedance Z_{eq} , in Figure 1(d), can be determined using (8). By substituting the expressions from (6) and (7) into (8), the result is given by (9).

$$Z_{eq} = \frac{1}{j\omega C_1} \parallel (R_{Ti} + j\omega L_{Ti}) \quad (8)$$

$$Z_{eq} = \frac{R_{Ti} + j\omega L_{Ti} \left(1 + \omega^2 C_1 L_{Ti} - \frac{C_1 R_{Ti}^2}{L_{Ti}} \right)}{(1 - \omega^2 C_1 L_{Ti})^2 + (\omega C_1 R_{Ti})^2} \quad (9)$$

The phase angle of Z_{eq} is derived from (9) and presented in (10).

$$\phi_{eq} = \tan^{-1} \left[\frac{\omega L_{Ti} \left(1 - \omega^2 L_{Ti} C_1 - \frac{C_1 R_{Ti}^2}{L_{Ti}} \right)}{R_{Ti}} \right] \quad (10)$$

Figure 2 illustrates the relationship between the phase angle (ϕ_{eq}) of Z_{eq} and the coupling coefficient (k). An optimal phase angle for achieving the ZVS condition is explained in the literature [21], [29], [30], and is shown in (11).

$$\phi_{opt} = \tan^{-1} \left(\frac{2}{\pi} \right) = 0.569 \text{ rad} = 32.48^\circ \quad (11)$$

The optimal phase angle (ϕ_{opt}) is calculated to be 32.48° . Figure 2 illustrates the correlation between ϕ_{eq} and the magnetic coupling coefficient (k). When k equals $k_{designed}$ (0.66), ϕ_{eq} matches ϕ_{opt} , achieving ZVS operation. This $k_{designed}$ value was determined through practical measurements. For coupling coefficients below $k_{designed}$, ϕ_{eq} exceeds ϕ_{opt} . Conversely, when k exceeds $k_{designed}$, ϕ_{eq} falls below ϕ_{opt} . At this point, the inverter transitions from ZVS to non-ZVS operation, making $k_{designed}$ the critical threshold for maintaining ZVS conditions. Therefore, the maximum magnetic coupling coefficient should be used in the design procedures to ensure ZVS mode of operation throughout any misalignment conditions.

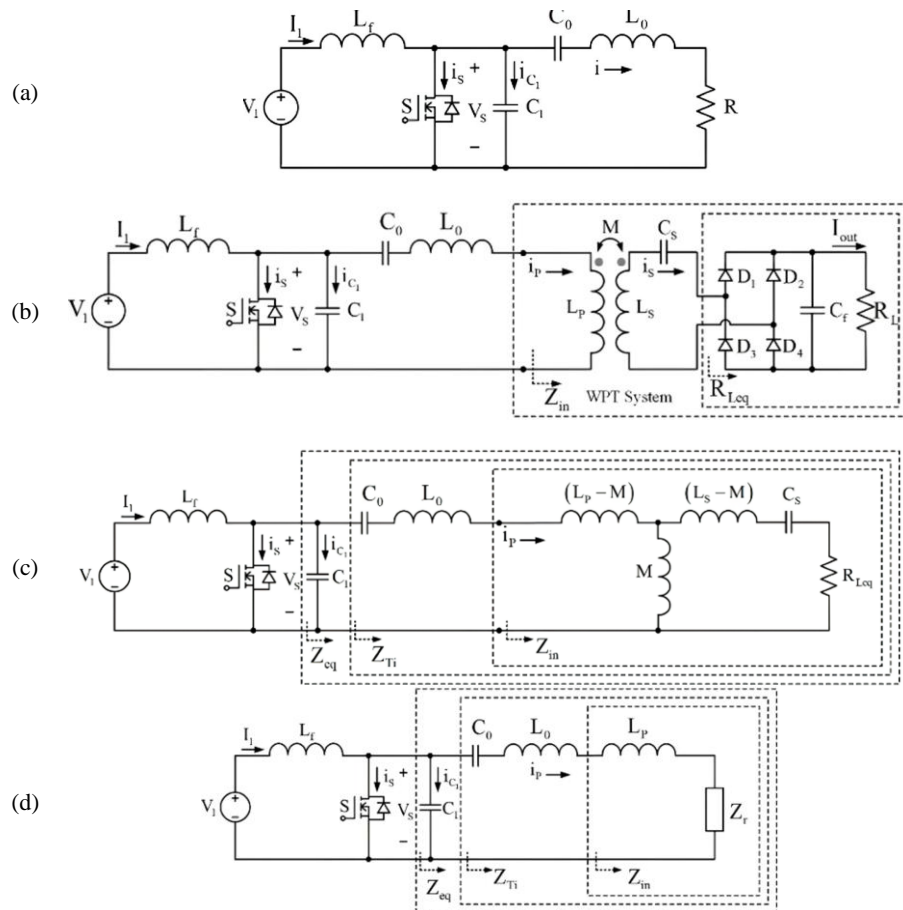


Figure 1. The WPT system's circuit: (a) standard single-ended resonant converter employing a Class-E-based switching scheme, (b) improved high-efficiency topology delivering power to a wireless transmission configuration, (c) simplified equivalent circuit of the WPT system, and (d) a further simplified model for impedance analysis

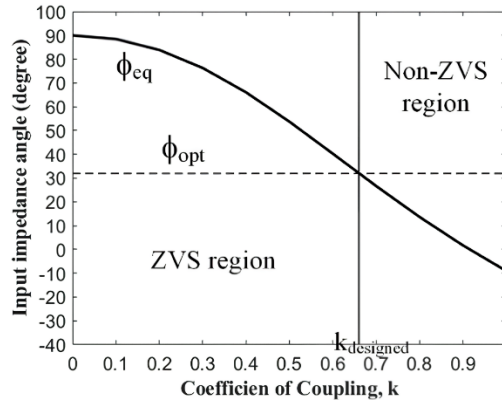


Figure 2. Relationship between phase angle (ϕ_{eq}) with the magnetic coupling coefficient (k)

2.1.2. Voltage and current analysis

The circuit in Figure 3 are used in the analysis. When the switching voltage in the switched-off state, that is, for $0 < \theta \leq \pi$ the shunt capacitance current can be represented as (12).

$$i_{C1}(\theta) = I_1 - I_m \sin(\theta + \phi) \quad (12)$$

Where I_1 represents the direct current input, I_m represents the magnitude of an output current, $\theta = \omega t$, which ω is angular switching frequency. $i_s(\theta)$ is the switch current that is equal to zero in the turned-off state. While turned-on state, specifically for $\pi < \theta \leq 2\pi$ the current $i_s(\theta)$ can be expressed as (13):

$$i_s(\theta) = I_1 - I_m \sin(\theta + \phi) \quad (13)$$

and $i_{C1}(\theta) = 0$. The switch voltage $v_s(\theta)$ for $0 < \theta \leq \pi$ equals an integral of the current flowing through the shunt capacitor $i_{C1}(\theta)$, represented by (14).

$$v_s(\theta) = \frac{1}{\omega C_1} \int_0^\theta i_{C1}(\theta') d\theta' \quad (14)$$

Thus, for $0 < \theta \leq \pi$, voltage across the switch $v_s(\theta)$ can be written as (15).

$$v_s(\theta) = \frac{I_1 \theta + I_m \cos(\theta + \phi) - I_m \cos \phi}{\omega C_1} \quad (15)$$

Satisfying the ZVS condition as derived from $v_s(\pi) = 0$, thus, from (15), yielding (16).

$$I_1 = \frac{2I_m}{\pi} \cos \phi \quad (16)$$

With no loss in the circuit, the input power equals the output power, that is $V_1 I_1 = I_m^2 R_{Ti} / 2$. Thus, I_m can be represented as (17).

$$I_m = \frac{4V_1}{\pi R_{Ti}} \cos \phi \quad (17)$$

Replace (17) with (16), and the DC current can be obtained as (18).

$$I_1 = \frac{8V_1}{\pi^2 R_{Ti}} \cos^2 \phi \quad (18)$$

Because the voltage at the choke inductor is zero, the DC input voltage can be expressed by (19).

$$V_1 = \frac{1}{2\pi} \int_0^{2\pi} v_s(\theta) d\theta' = -\frac{2V_1 \sin 2\phi}{\pi^2 \omega C_1 R_{Ti}} \quad (19)$$

Hence, as in (20).

$$\omega C_1 R_{Ti} = -\frac{2 \sin 2\phi}{\pi^2} \quad (20)$$

The phase angle (ϕ) in (20) can be determined by assuming the system is no loss. Therefore, the output power matches the DC input as shown in (21).

$$P_{out} = V_1 I_1 = \frac{8V_1^2}{\pi^2 R_{Ti}} \cos^2 \phi \quad (21)$$

Thus, the phase angle (ϕ) can be given by (22).

$$\phi = \cos^{-1} \left(\frac{\pi}{V_1} \sqrt{\frac{P_{out} R_{Ti}}{8}} \right) \quad (22)$$

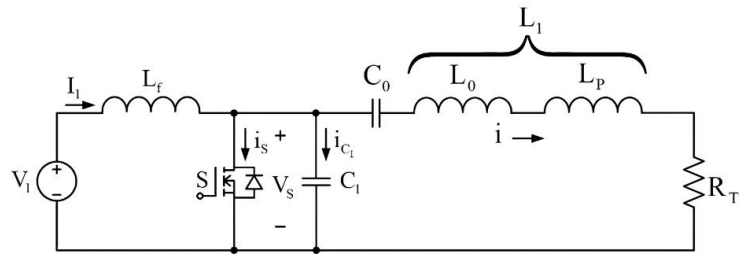


Figure 3. The simplified circuit model representing the Class-E inverter combined with the WPT system

2.2. Designed circuit parameters

In this section, the parameters in the circuit are designed through corresponding formulas. The resistive load (R_L) for the WPT system, as shown in Figure 1, is calculated using the relationship between V_{out} and I_{out} , as given in (23).

$$R_L = \frac{V_{out}}{I_{out}} \quad (23)$$

The rectifier and its resistive load are modeled as an equivalent AC resistance (R_{Leq}), as illustrated in Figures 1(b) and 1(c).

$$R_{Leq} = \frac{8R_L}{\pi^2} \quad (24)$$

The secondary compensation capacitor C_s is calculated based on the expression provided in (25).

$$C_s = \frac{1}{4\pi f_s^2 L_s} \quad (25)$$

The total primary-side inductance (L_1) can be expressed as a combination of the inductances L_0 and L_p , as defined in (26).

$$L_1 = \frac{Q_L R_{Ti}}{\omega_0} \quad (26)$$

In (26), Q_L represents the quality factor, and ω_0 is defined as $2\pi f_s$, where f_s represents the switching frequency. The inductance (L_0) is calculated using (27).

$$L_0 = L_1 - L_p \quad (27)$$

Replacing (22) into (20), the C_1 can be presented by (28).

$$C_1 = -\frac{2 \sin 2 \left(\cos^{-1} \left(\frac{\pi}{V_{dc}} \sqrt{\frac{P_{out} R_{Ti}}{8}} \right) \right)}{\omega_0 \pi^2 R_{Ti}} \quad (28)$$

The value of resonant capacitor (C_0) can be expressed in (29).

$$C_0 = \frac{1}{\omega(R_{reflected} Q_L - X)} \quad (29)$$

Where $X = R_{reflected} \left(\cot \phi - \frac{\pi^2}{4} \operatorname{cosec} 2\phi \right)$ [24]. The choke inductance (L_f) can be determined by (30).

$$L_f = 2 \left(\frac{\pi^2}{4} + 1 \right) \frac{R_{reflected}}{f_s} \quad (30)$$

The DC input voltage (V_i) can be calculated by (31).

$$V_i = \sqrt{\frac{R_{reflected}(\pi^2 + 4)}{8}} \quad (31)$$

2.3. Modes of operation

The mode of operation under optimal conditions is presented in Figure 4, alongside the associated electrical signals derived from the configuration in Figure 1(b). Its behavior can be divided into nine distinct operational modes, with Figure 5 providing a description of the switching operation for each mode:

- Mode 1 [$t_0 - t_1$]: Activation by gating voltage (v_{GS}) triggers a power switch. This action enables the switch current (i_S) to reverse its direction and pass through the antiparallel diode. Concurrently, transmitter current (i_P) flows positively, while receiver current (i_S) flows negatively. When diodes D_2 and D_3 conduct simultaneously, the resulting receiver voltage v_2 becomes negative (Figure 5(a)).
- Mode 2 [$t_1 - t_2$]: The switching device stays conducting. At t_2 , current i_S through the switch reverses to a positive direction. During this interval, the transmitter current i_P and receiver current i_S exhibit no significant change. The transmitter-side voltage v_2 continues to exhibit negative polarity (Figure 5(b)).
- Mode 3 [$t_2 - t_3$]: The switching element continues conducting, enabling a forward current flow (i_S). During this phase, the transmitter current (i_P) reverses and takes on a negative polarity. In contrast, the receiver current (i_S) shows no variation, and the transmitter voltage (v_2) maintains its negative level (Figure 5(c)).
- Mode 4 [$t_3 - t_4$]: The power switch continues conducting, enabling the current i_S to flow in the forward direction. In parallel, the transmitter current i_P retains its positive flow. From time t_3 onward, the receiver current i_S is redirected through diodes D_1 and D_4 , resulting in a rise of the receiver voltage v_2 to a positive level (Figure 5(d)).
- Mode 5 [$t_4 - t_5$]: At t_4 , the gate signal v_{GS} drops to zero, deactivating the power switch. As a result, the shunt capacitor C_1 begins charging from the supply. During this interval, the transmitter current i_P reverses direction and becomes negative, while the receiver current i_S continues to flow forward via diodes D_1 and D_4 , sustaining a positive receiver-side voltage v_2 . Although i_P flows oppositely, i_S maintains its direction, ensuring that v_2 remains positive (Figure 5(e)).
- Mode 6 [$t_5 - t_6$]: While the switching element stays non-conducting, capacitor C_1 continues accumulating charge from the input supply. At t_5 , the transmitter current i_P begins to flow in the forward direction. Simultaneously, the receiver current i_S sustains its positive flow through diodes D_1 and D_4 , maintaining a positive voltage across the receiver side v_2 (Figure 5(f)).
- Mode 7 [$t_6 - t_7$]: With the power switch remaining inactive, the shunt capacitor C_1 begins discharging. At this stage, the transmitter current i_P flows in the forward direction, while the receiver current i_S continues its positive path through diodes D_1 and D_4 , thereby sustaining a positive voltage across the receiver side v_2 (Figure 5(g)).
- Mode 8 [$t_7 - t_8$]: The power switch stays in the off state, permitting the shunt capacitor C_1 to discharge. During this interval, the transmitter current i_P maintains its forward direction. Meanwhile, at t_7 , the receiver current i_S starts flowing in the reverse direction via diodes D_2 and D_3 , leading to a negative voltage across the receiver side v_2 (Figure 5(h)).
- Mode 9 [$t_8 - t_9$]: The power switch stays in the off state. At t_8 , the shunt capacitor C_1 completes its discharge, directing current via the intrinsic diode path within the switching device. Consequently, a reverse-direction current i_S is conducted, establishing zero-voltage switching (ZVS) conditions. During this time, the transmitter current i_P remains constant, and the receiver voltage v_2 retains its negative value (Figure 5(i)). The switching cycle then proceeds back to Mode 1.

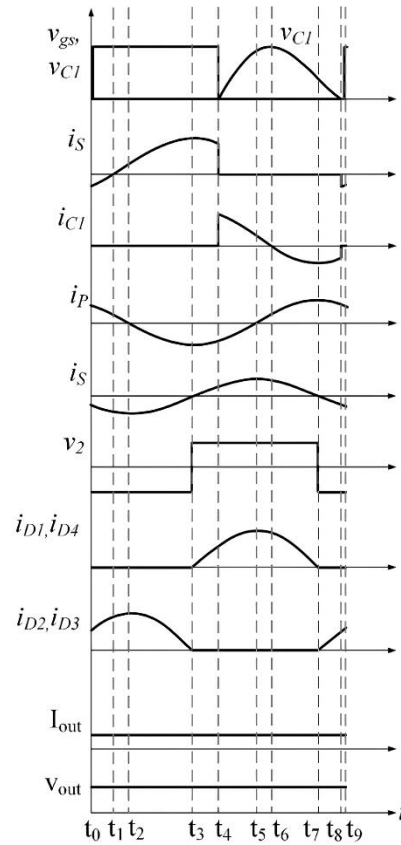


Figure 4. Waveforms related to the modes of operation for analysis

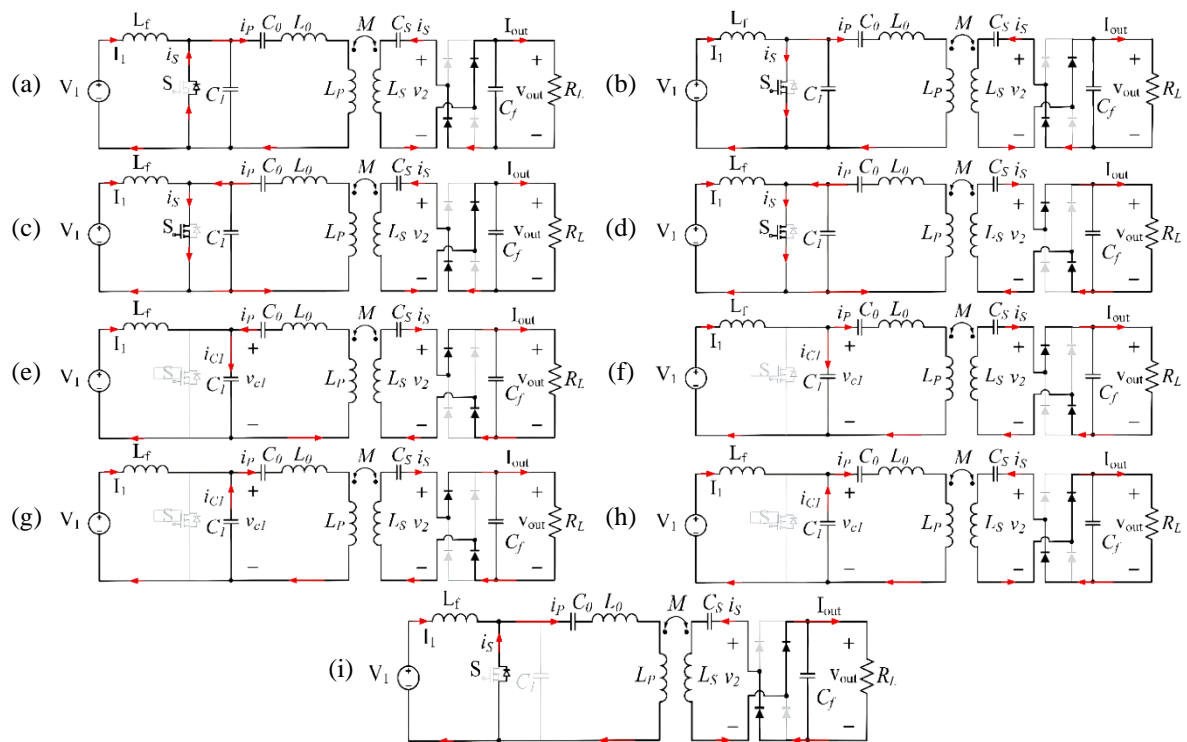


Figure 5. Switching sequence representation for each operating condition: nine-stage operating sequence:

(a) Mode 1, (b) Mode 2, (c) Mode 3, (d) Mode 4, (e) Mode 5, (f) Mode 6, (g) Mode 7,

(h) Mode 8, and (i) Mode 9 are the corresponding to time intervals $t_0 - t_9$ as described in the main text

3. STUDY RESULTS

This section provides a detailed overview of the simulation and experimental results. A prototype for untethered energy transmission utilizing a resonant-mode Class-E converter topology was developed following the proposed design framework.

3.1. Parameter design

A wireless power prototype is developed to verify the proposed method for transferring power to a load: a 3,400 mAh lithium-ion battery delivering 4.2 V at its terminals and accepting a 2 A charge input. This battery's load resistance is considered constant. From the simulation, which examines the battery's state of charge (SOC) between 20% to 80%, it was found that the internal resistance remains relatively constant. Therefore, a load resistance of 2.1 Ω is selected for the study. The transmitter and receiver coils consist of conductors placed on square ferrite cores, each measuring 5.3 cm by 5.3 cm, with an inductance of 6.25 μ H per coil. The magnetic coupling coefficient at an aligned distance of 1 cm between the coils is 0.66, which is used as the design value. The remaining parameters were calculated using the equations from section 2.3. The obtained circuit parameters are summarized as follows: an equivalent resistance $R_{Leq} = 1.702 \Omega$, a compensation capacitor $C_2 = 64.845$ nF, a reflected resistance $R_{reflected} = 21.41 \Omega$, a resonant inductance $L_0 = 266.35 \mu$ H, and two capacitances $C_1 = 5.9893$ nF and $C_0 = 1.5957$ nF.

3.2. Simulation results

By employing the circuit layout depicted in Figure 1(b), simulations were conducted for cases where $k = k_{designed}$, $k < k_{designed}$, and $k > k_{designed}$. In this design, $k_{designed}$ represents the optimal value, empirically determined to be 0.66. The corresponding results are presented in Figure 6. The first set of measurements was collected for $k = k_{designed} = 0.66$. Afterward, the measurements were performed again by modifying the horizontal misalignment and a separation between coils to achieve cases where $k < k_{designed}$ and $k > k_{designed}$. The misalignment has affected the WPT system's efficiency, as discussed in [31]-[35]. In parallel, enhanced system efficiency under varying coupling and alignment conditions has also been explored in [36]-[38].

Figure 6(a) illustrates the gate-to-source voltage (V_{GS}) waveform and switching voltage (V_{DS}) waveform across the drain and source terminals. In Figure 6(a), the V_{GS} waveform is scaled by a factor of 75 for clarity. The zero-voltage switching (ZVS) point is indicated with a small negative switch voltage, showing that the v_{DS} reduces to zero prior to the switch activation, achieving the ZVS condition. Figure 6(b) illustrates the simulation results for $k < k_{designed} = 0.51$. The voltage waveform V_{DS} becomes narrower and exhibits a higher voltage amplitude. The inverter operates under ZVS conditions, consistent with the analysis in section 2.1.1, which states that ZVS can be achieved when $k < k_{designed}$. The simulations were performed for $k > k_{designed} = 0.84$. The results, presented in Figure 6(c), indicates that the inverter operates in a non-zero-voltage condition. This phenomenon occurred because the magnetic coupling coefficient exceeded the optimal value, as discussed in subsection 2.1.1. Finally, Figure 6(d) presents the simulation results for $k > k_{designed} = 0.9$. At this coupling coefficient, the overlap between the V_{DS} and V_{GS} waveforms confirms that the inverter still operated in a non-ZVS condition.

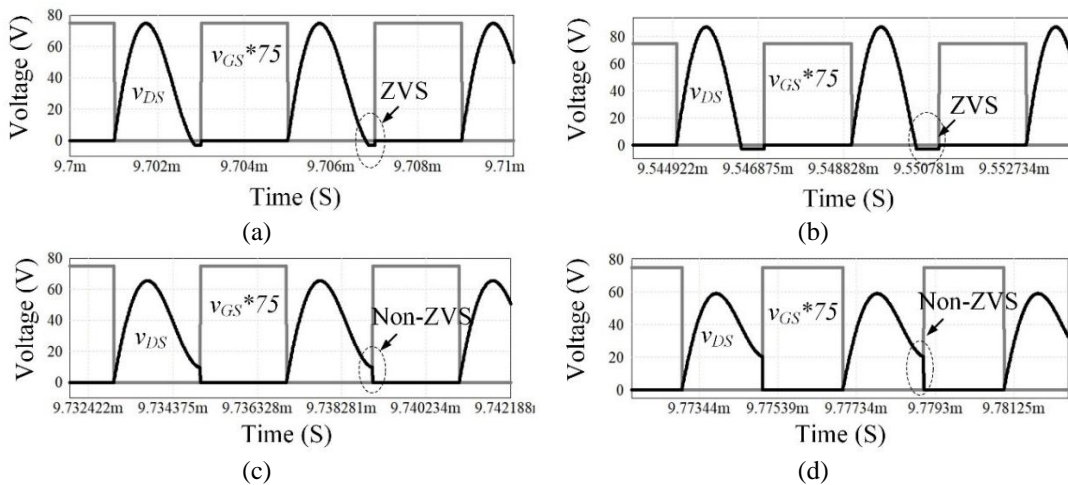


Figure 6. The switching voltage (V_{DS}) and gate-to-source voltage (V_{GS}) under different coupling conditions: (a) $k = k_{designed} = 0.66$; (b) $k < k_{designed} = 0.51$; (c) $k > k_{designed} = 0.84$; and (d) $k > k_{designed} = 0.9$

The simulated outcomes align with the analytical findings outlined under section 2.1.1. The observed ZVS and non-ZVS switching behaviors in Figure 6 correspond directly to the calculated phase angle ϕ_{eq} in each case. When $k = k_{\text{designed}}$, the phase angle approaches the optimal ϕ_{opt} , resulting in ZVS operation. In contrast, deviation from k_{designed} leads to a phase angle mismatch, explaining the deterioration of ZVS conditions as predicted by the analytical model.

3.3. Experimental results

Figure 7 illustrates the experimental setup, detailing the arrangement of equipment and the procedures used to conduct the tests and gather data. In the experimental setup, the coil separation distance and misalignment were tuned to reach the desired level of coupling coefficient. The first set of measurements was taken with $k = k_{\text{designed}} = 0.66$. The experiment was then repeated with adjustments to the coil misalignment and separation between coils to achieve $k < k_{\text{designed}} = 0.51$, $k > k_{\text{designed}} = 0.84$, and $k > k_{\text{designed}} = 0.9$. In the experimental configuration, a 20 V DC supply was used to drive the inverter, operating at 250 kHz with a 50% duty cycle. Power was wirelessly delivered to a resistive load located on the secondary side of the circuit. The coils were accurately aligned with a 1 cm spacing, yielding a magnetic coupling coefficient of 0.66 under the initial test condition. Waveforms of V_{DS} and V_{GS} were captured using an oscilloscope, as depicted in Figure 8(a). The observed ZVS behavior of V_{DS} and V_{GS} correlates well with the simulated data (see Figure 6(a)). An output power of 10 W was successfully transferred to the output stage, in alignment with the intended design criteria. The input power associated with this condition was recorded at 10.5 W, resulting in an overall efficiency of 95%. The coil misalignment was adjusted to gain a magnetic coupling coefficient of 0.51. Figure 8(b) presents the experimental results for the switching voltage (V_{DS}) and gate-to-source voltage (V_{GS}), which closely align with simulation results, as illustrated in Figure 6(b). Inverter continued to operate under zero-voltage switching (ZVS), delivering an average of 8.85 W at the output, while drawing approximately 10.17 W at the input, resulting in an overall efficiency of 84%. Figure 8(c) presents the experimental results for $k = 0.84$. Under this condition, the inverter demonstrated non-optimal performance, as the ZVS condition was not met. Measured output power was 8 W, whereas the measured input power was 9.1 W, resulting in an overall efficiency of 88%. Likewise, Figure 8(d) depicts the experimental result obtained for $k = 0.9$. The average output power was measured at 7.31 W, with the average input power measured at 8.6 W, resulting in an overall efficiency of 85%. Efficiency decreases due to losses caused by the overlapping of switch voltage and current signals.

The study reveals that when designing the WPT system powered by the Class-E inverter for operating under ZVS conditions, the maximum value of the magnetic coupling coefficient should be used in the design process. This approach ensures that the system operates under ZVS as long as k remains within the condition $k < k_{\text{designed}}$. However, even though the inverter can maintain ZVS operation when k is less than k_{designed} , the output power may deviate from the designed value due to weak coupling. Experimental results indicate that when k drops to 0.51 or below, the output power falls below 9 watts.

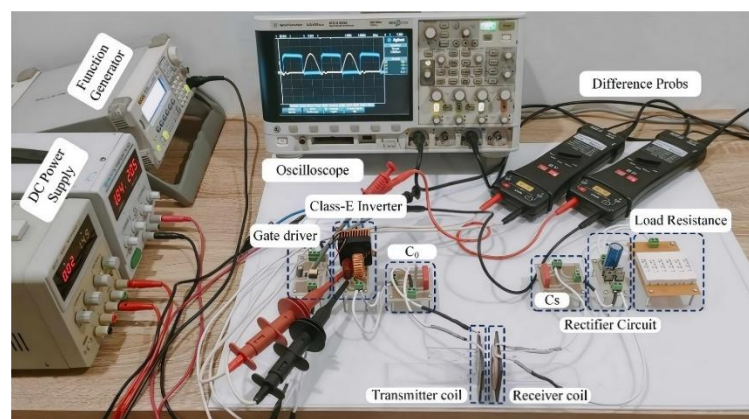


Figure 7. The layout of the experimental setup and the arrangement of equipment

These experimental results are in line with the theoretical ZVS operation zones identified in section 2.1.1. Specifically, when the coupling coefficient equals the designed value $k = 0.66$, the measured V_{DS} waveform confirms that ZVS is achieved, as predicted by the phase angle ϕ_{eq} reaching the optimal value ϕ_{opt} . A reduction in the coupling factor to $k = 0.51$ allows the inverter to maintain ZVS operation, as predicted by

the model where $\phi_{eq} > \phi_{opt}$. This condition still satisfies ZVS, but results in reduced output power due to weaker magnetic coupling. For cases where $k > 0.66$, such as $k = 0.84$ and $k = 0.9$, the V_{DS} waveform overlaps with V_{GS} , indicating that ZVS is no longer achieved. This confirms the theoretical prediction in section 2.1.1, where $\phi_{eq} < \phi_{opt}$, violating the ZVS condition. The measured efficiencies also correlate with these switching conditions: highest under ZVS (95% at $k = 0.66$) and reduced under non-ZVS due to simultaneous voltage-current overlap, causing switching losses.

The experimental waveforms also support the theoretical model in section 2.1.1, where the coupling coefficient variation affects the phase angle ϕ_{eq} , thus impacting the ZVS condition. The decline in efficiency in the cases of misalignment further confirms the model's prediction.

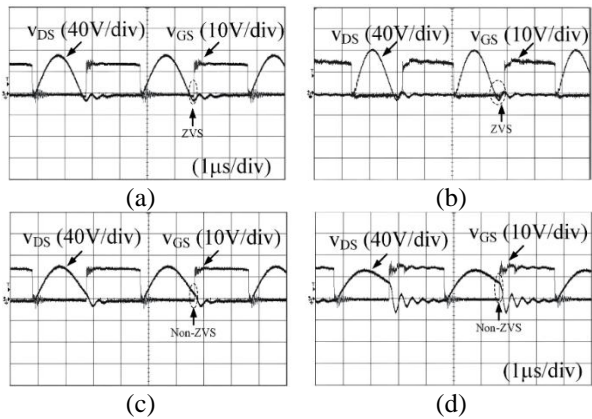


Figure 8. Switching voltage (V_{DS}) and gate-to-source voltage (V_{GS}) from experimental measurements under different coupling conditions: (a) $k = k_{\text{designed}}$, (b) $k < k_{\text{designed}} = 0.51$, (c) $k > k_{\text{designed}} = 0.84$, and (d) $k > k_{\text{designed}}$.

4. CONCLUSION

This work introduces a novel framework for designing Class-E-based converters utilized in contactless energy delivery applications, aiming to ensure soft-switching performance over various levels of magnetic coupling. The proposed strategy analytically links the phase angle and coupling coefficient to ZVS conditions and uses the maximum expected coupling coefficient as a critical design parameter to ensure robust ZVS operation, even under coil misalignment. Simulation and experimental results confirm that the inverter satisfies ZVS for $0 < k \leq k_{\text{designed}}$, with peak efficiency reaching 95%. The proposed method offers practical value for varying coupling scenarios, aiding in enhancing the design of dependable and high-performance wireless energy transfer solutions.

FUNDING INFORMATION

The author gratefully acknowledges the Fundamental Fund (FF2568), provided by Rajamangala University of Technology Lanna, under grant number FF2568P123, which supported this project.

AUTHOR CONTRIBUTIONS STATEMENT

This journal uses the Contributor Roles Taxonomy (CRediT) to recognize individual author contributions, reduce authorship disputes, and facilitate collaboration.

| Name of Author | C | M | So | Va | Fo | I | R | D | O | E | Vi | Su | P | Fu |
|------------------|---|---|----|----|----|---|---|---|---|---|----|----|---|----|
| Anon Namin | ✓ | ✓ | | ✓ | ✓ | ✓ | ✓ | ✓ | ✓ | ✓ | ✓ | ✓ | ✓ | ✓ |
| Chuchat Donloei | | ✓ | ✓ | | ✓ | ✓ | | | ✓ | | ✓ | ✓ | | |
| Ekkachai Chaidee | ✓ | ✓ | ✓ | ✓ | ✓ | ✓ | ✓ | ✓ | ✓ | ✓ | ✓ | ✓ | ✓ | ✓ |

| | | |
|-----------------------|--------------------------------|----------------------------|
| C : Conceptualization | I : Investigation | Vi : Visualization |
| M : Methodology | R : Resources | Su : Supervision |
| So : Software | D : Data Curation | P : Project administration |
| Va : Validation | O : Writing - Original Draft | Fu : Funding acquisition |
| Fo : Formal analysis | E : Writing - Review & Editing | |

CONFLICT OF INTEREST STATEMENT

Authors state no conflict of interest.

DATA AVAILABILITY

The authors confirm that the data supporting the findings of this study are available within the article.




REFERENCES

- [1] G. L. Barbruni, P. M. Ros, D. Demarchi, S. Carrara, and D. Ghezzi, "Miniaturised wireless power transfer systems for neurostimulation: a review," *IEEE Transactions on Biomedical Circuits and Systems*, vol. 14, no. 6, pp. 1160–1178, Dec. 2020, doi: 10.1109/TBCAS.2020.3038599.
- [2] S. Roy, A. N. M. W. Azad, S. Baidya, M. K. Alam, and F. Khan, "Powering solutions for biomedical sensors and implants inside the human body: A comprehensive review on energy harvesting units, energy storage, and wireless power transfer techniques," *IEEE Transactions on Power Electronics*, vol. 37, no. 10, pp. 12237–12263, Oct. 2022, doi: 10.1109/TPEL.2022.3164890.
- [3] H. Le-Huu, G. T. Bui, and C. Seo, "Efficient compact radiative near-field wireless power transfer to miniature biomedical implants," *IEEE Antennas and Wireless Propagation Letters*, vol. 22, no. 12, pp. 2803–2807, Dec. 2023, doi: 10.1109/LAWP.2023.3298350.
- [4] Z. Liu, Y. Su, Y. Zhao, A. P. Hu, and X. Dai, "Capacitive power transfer system with double T-type resonant network for mobile devices charging/supply," *IEEE Transactions on Power Electronics*, vol. 37, no. 2, pp. 2394–2403, 2022, doi: 10.1109/TPEL.2021.3105406.
- [5] Q. Huang, Z. Ma, S. Wang, and Y. Yang, "Integration of near-field communication (NFC) antenna and wireless charging coil for portable electronic products," *IEEE Journal of Emerging and Selected Topics in Power Electronics*, vol. 12, no. 4, pp. 3415–3425, Aug. 2024, doi: 10.1109/JESTPE.2024.3385028.
- [6] C. Teeneti *et al.*, "System-level approach to designing a smart wireless charging system for power wheelchairs," *IEEE Transactions on Industry Applications*, vol. 57, no. 5, pp. 5128–5144, Sep. 2021, doi: 10.1109/TIA.2021.3093843.
- [7] A. Azad, R. Tavakoli, U. Pratik, B. Varghese, C. Coopmans, and Z. Pantic, "A smart autonomous WPT system for electric wheelchair applications with free-positioning charging feature," *IEEE Journal of Emerging and Selected Topics in Power Electronics*, vol. 8, no. 4, pp. 3516–3532, Dec. 2020, doi: 10.1109/JESTPE.2018.2884887.
- [8] A. Mahesh, B. Chokkalingam, and L. Mihet-Popa, "Inductive wireless power transfer charging for electric vehicles—a review," *IEEE Access*, vol. 9, pp. 137667–137713, 2021, doi: 10.1109/ACCESS.2021.3116678.
- [9] E. Chaidce, A. Sangswang, S. Naetiladdanon, and S. Nutwong, "An inverter topology for multitransmitter wireless power transfer systems," *IEEE Access*, vol. 10, pp. 36592–36605, 2022, doi: 10.1109/ACCESS.2022.3162906.
- [10] P. Machura, V. De Santis, and Q. Li, "Driving range of electric vehicles charged by wireless power transfer," *IEEE Transactions on Vehicular Technology*, vol. 69, no. 6, pp. 5968–5982, Jun. 2020, doi: 10.1109/TVT.2020.2984386.
- [11] H. Li, K. Wang, J. Fang, and Y. Tang, "Pulse density modulated ZVS full-bridge converters for wireless power transfer systems," *IEEE Transactions on Power Electronics*, vol. 34, no. 1, pp. 369–377, Jan. 2019, doi: 10.1109/TPEL.2018.2812213.
- [12] X. Zhu *et al.*, "High-efficiency WPT system for CC/CV charging based on double-half-bridge inverter topology with variable inductors," *IEEE Transactions on Power Electronics*, vol. 37, no. 5, pp. 2437–2448, 2021, doi: 10.1109/TPEL.2021.3107461.
- [13] T. Dinc, S. Kalia, S. Akhtar, B. Haroun, B. Cook, and S. Sankaran, "High-efficiency Class-E power amplifiers for mmWave radar sensors: design and implementation," *IEEE Journal of Solid-State Circuits*, vol. 57, no. 5, pp. 1291–1299, May 2022, doi: 10.1109/JSSC.2022.3147723.
- [14] H. Li, C. Wang, Y. Liu, and R. Yue, "Research on single-switch wireless power transfer system based on SiC MOSFET," *IEEE Access*, vol. 7, pp. 163796–163805, 2019, doi: 10.1109/ACCESS.2019.2952463.
- [15] A. Kuperman, U. Levy, J. Goren, A. Zafransky, and A. Savernin, "Battery charger for electric vehicle traction battery switch station," *IEEE Transactions on Industrial Electronics*, vol. 60, no. 12, pp. 5391–5399, Dec. 2013, doi: 10.1109/TIE.2012.2233695.
- [16] A. Komanaka, W. Zhu, X. Wei, K. Nguyen, and H. Sekiya, "Load-independent inverse class-E ZVS inverter and its application to wireless power transfer systems," *IET Power Electronics*, vol. 15, no. 7, pp. 644–658, May 2022, doi: 10.1049/pel2.12256.
- [17] T. Sensui and H. Koizumi, "Load-independent Class E zero-voltage-switching parallel resonant inverter," *IEEE Transactions on Power Electronics*, vol. 36, no. 11, pp. 12805–12818, Nov. 2021, doi: 10.1109/TPEL.2021.3077077.
- [18] X. Huang, Z. Yu, Y. Dou, S. Lin, Z. Ouyang, and M. A. E. Andersen, "Load-independent push-pull Class E2 topology with coupled inductors for MHz-WPT applications," *IEEE Transactions on Power Electronics*, vol. 37, no. 7, pp. 8726–8737, Jul. 2022, doi: 10.1109/TPEL.2022.3150175.
- [19] L. He and D. Guo, "A clamped and harmonic injected Class-E converter with ZVS and reduced voltage stress over wide range of distance in WPT system," *IEEE Transactions on Power Electronics*, vol. 36, no. 6, pp. 6339–6350, Jun. 2021, doi: 10.1109/TPEL.2020.3038562.
- [20] J. Zhang, J. Zhao, L. Mao, J. Zhao, Z. Jiang, and K. Qu, "ZVS operation of Class-E inverter based on secondary side zero compensation switching at variable coupling coefficient in WPT," *IEEE Transactions on Industry Applications*, vol. 58, no. 1, pp. 1022–1031, Jan. 2022, doi: 10.1109/TIA.2021.3125916.
- [21] L. He and D. Guo, "Compound voltage clamped Class-E converter with ZVS and flexible power transfer for WPT system," *IEEE Transactions on Power Electronics*, vol. 35, no. 7, pp. 7123–7133, Jul. 2020, doi: 10.1109/TPEL.2019.2954078.
- [22] F. Issi and O. Kaplan, "Design and application of wireless power transfer using Class-E inverter based on adaptive impedance-matching network," *ISA Transactions*, vol. 126, pp. 415–427, 2022, doi: 10.1016/j.isatra.2021.07.050.
- [23] M. M. Ahmadi, S. Pezeshkpour, and Z. Kabirkhoo, "A high-efficiency ASK-modulated Class-E power and data transmitter for medical implants," *IEEE Transactions on Power Electronics*, vol. 37, no. 1, pp. 1090–1101, Jan. 2022, doi: 10.1109/TPEL.2021.3092829.
- [24] H. Li, Y. Yang, J. Chen, J. Xu, M. Liu, and Y. Wang, "A hybrid Class-E topology with constant current and constant voltage output for light EVs wireless charging application," *IEEE Transactions on Transportation Electrification*, vol. 7, no. 4, pp. 2168–2180, Dec. 2021, doi: 10.1109/TTE.2021.3083363.
- [25] W. Zhu, Y. Komiyama, K. Nguyen, and H. Sekiya, "Comprehensive and simplified numerical design procedure for Class-E switching circuits," *IEEE Access*, vol. 9, pp. 149971–149981, 2021, doi: 10.1109/ACCESS.2021.3119039.




- [26] F. Corti, A. Reatti, Y.-H. Wu, D. Czarkowski, and S. Musumeci, "Zero voltage switching condition in Class-E inverter for capacitive wireless power transfer applications," *Energies*, vol. 14, no. 4, p. 911, Feb. 2021, doi: 10.3390/en14040911.
- [27] T. Suetsugu and M. K. Kazimierczuk, "Design procedure of Class-E amplifier for off-nominal operation at 50% duty ratio," *IEEE Transactions on Circuits and Systems I: Regular Papers*, vol. 53, no. 7, pp. 1468–1476, Jul. 2006, doi: 10.1109/TCSI.2006.875181.
- [28] H. Sekiya, K. Tokano, W. Zhu, Y. Komiyama, and K. Nguyen, "Design procedure of load-independent Class-E WPT systems and its application in robot arm," *IEEE Transactions on Industrial Electronics*, vol. 70, no. 10, pp. 10014–10023, Oct. 2023, doi: 10.1109/TIE.2022.3220818.
- [29] T. P. G. van Nunen, R. M. C. Mestrom, and H. J. Visser, "Wireless power transfer to biomedical implants using a Class-E inverter and a Class-DE rectifier," *IEEE Journal of Electromagnetics, RF and Microwaves in Medicine and Biology*, vol. 7, no. 3, pp. 202–209, Sep. 2023, doi: 10.1109/JERM.2023.3267042.
- [30] M. K. Kazimierczuk and D. Czarkowski, *Resonant power converters*, 2nd ed. John Wiley & Sons, 2012.
- [31] I. Casaucao, A. Triviño, and A. Delgado, "Ferromagnetic design of coils considering misalignment effects for a SAE J2954-Compliant EV Wireless Charger," *IEEE Access*, vol. 12, pp. 163978–163987, 2024, doi: 10.1109/ACCESS.2024.3492350.
- [32] F. Abderrazak, E. Antonino-Daviu, L. Talbi, and M. Ferrando-Bataller, "Characteristic modes analyses for misalignment in wireless power transfer system," *IEEE Access*, vol. 12, pp. 65007–65023, 2024, doi: 10.1109/ACCESS.2024.3397249.
- [33] J. C. Quirós, E. V. Guerrero, J. K. Sangeno, and A. Triviño, "Magnetic integration of circular pads and lcc-lcc for ev wireless charging tolerant to misalignment," *IEEE Access*, vol. 11, pp. 98558–98565, 2023, doi: 10.1109/ACCESS.2023.3312008.
- [34] U. Kamnam, A. Namin, P. Wuttiwai, J. Yodwong, P. Thounthong, and N. Takorabet, "Dynamic and steady-state behavior of distributed power supply in DC architecture with minimized DC bus capacitor," *IEEE Journal of Industry Applications*, vol. 12, no. 4, pp. 745–754, 2023, doi: 10.1541/ieejia.22008110.
- [35] S. Nutwong, A. Sangswang, and S. Naetiladdanon, "An inverter topology for wireless power transfer system with multiple transmitter coils," *Applied Sciences*, vol. 9, no. 8, p. 1551, Apr. 2019, doi: 10.3390/app9081551.
- [36] W. En-Naghma, H. Halaq, and A. El Ougli, "Analysis, design, and optimization based on genetic algorithms of a highly efficient dual-band rectenna system for radiofrequency energy-harvesting applications," *Results in Engineering*, vol. 23, p. 102739, Sep. 2024, doi: 10.1016/j.rineng.2024.102739.
- [37] E.-N. Walid, H. Hanan, and E. O. Abdelghani, "An improvement performance of a novel triple-band microstrip antenna design based on a hexagonal patch and truncation in the ground for RF energy harvesting systems," in *2024 International Conference on Circuit, Systems and Communication (ICCSC)*, IEEE, Jun. 2024, pp. 1–4. doi: 10.1109/ICCSC62074.2024.10616570.
- [38] W. En-naghma, M. Latrach, H. Halaq, and A. El Ougli, "An experimental study of a high-gain, wideband circularly polarized printed antenna array at 2.45 GHz in the ISM band for wireless power transmission applications," *Scientific African*, vol. 27, p. e02619, Mar. 2025, doi: 10.1016/j.sciaf.2025.e02619.

BIOGRAPHIES OF AUTHORS






Anon Namin    is an Assistant Professor in the Department of Electrical Engineering, Faculty of Engineering, Rajamangala University of Technology Lanna (RMUTL), Chiang Rai, Thailand. He received the B.Sc.Ind.Ed. in Electrical Engineering from King Mongkut's Institute of Technology Thonburi, Bangkok, Thailand, in 1996. His M.Sc.Ind.Ed. in Electrical Engineering and Ph.D. in Energy Technology were finished at King Mongkut's Institute of Technology Thonburi (KMUTT), Thailand, in 2002 and 2013, respectively. His main research interests include power electronic circuits and control, inductive wireless power transfer, wireless EV charging, solar simulator, and photovoltaic characterization. He can be contacted at email: anamin@rmutl.ac.th.



Chuchat Donloei    received his B.Eng. in the Department of Electrical Engineering, Faculty of Engineering, Rajamangala University of Technology Lanna (RMUTL), Chiang Rai in 2015. He is currently pursuing the M.Eng. degree in Electrical Engineering of the Rajamangala University of Technology Lanna (RMUTL). His research interests include the field of wireless power transfer, resonant inverter, power electronics, and control. He can be contacted at email: chuchat_do65@live.rmutl.ac.th.



Ekkachai Chaidee    is an Assistant Professor and a lecturer in the Department of Electrical Engineering, Faculty of Engineering at the Rajamangala University of Technology Lanna (RMUTL), Chiang Rai, Thailand. He received his B.Sc.Ind.Ed. degree in electrical engineering from the King Mongkut's University of Technology Thonburi (KMUTT), Bangkok, Thailand, in 2001, the M.Sc. (Eng.) degree in electrical engineering from the King Mongkut's University of Technology North Bangkok (KMUTNB), Bangkok, Thailand, in 2008, and D.Eng. degree in electrical and information engineering technology (KMUTT), Bangkok, Thailand, in 2022. His research interests include the field of the resonant inverter, wireless power transfer, power electronics, and control. He can be contacted at email: ekkachai@rmutl.ac.th.